Additive Manufacturing 40 (2021) 101922

Contents lists available at ScienceDirect

Additive Manufacturing

journal homepage: www.elsevier.com/locate/addma

Research Paper

Prediction of the deformed geometry of vat photo-polymerized components using a multi-physical modeling framework

S. Westbeek [a,b], J.J.C. Remmers [a,*], J.A.W. van Dommelen [a], H.H. Maalderink [b], M.G.D. Geers [a]

[a] Eindhoven University of Technology, Department of Mechanical Engineering, P.O. Box 513, 5600 MB Eindhoven, The Netherlands
[b] TNO Holst Centre, High Tech Campus 31, 5605 KN Eindhoven, The Netherlands

ARTICLE INFO

Keywords:
Additive manufacturing
Vat photopolymerization
Digital light processing
Multi-physical modeling
Process simulation
Validation study
Mechanical analysis

ABSTRACT

In photopolymerization-based additive manufacturing a complex interplay exists between the vat photo-polymerization process characteristics and the (photo-active) resin's material properties, which governs the trajectory from the input target geometry to the resulting true geometry of a printed component. Particularly for fine featured geometries, there might be a clear mismatch between the latter two. Determining whether the entire component is printable can only be properly assessed through a test-print. The current work proposes an alternative modeling-driven route, which, after system and material characterization, facilitates predicting the geometrical defects of the resulting solidified component (including deformation). This is enabled through a coupled multi-physical modeling of irradiation, photopolymerization, solidification and chemical shrinkage.

1. Introduction

Vat photopolymerization (VP) is an additive manufacturing (AM) technique capable of fabricating highly accurate polymer components with high speed. The additive process is based on selective irradiation of a photo-active polymer resin by (near) UV light in a layer-by-layer fashion. The relatively low energy input induces a chemical photo-polymerization reaction, which in turn causes solidification. Even though the concept of VP might appear more suitable for rapid prototyping, high performance materials with tailored properties for a wide variety of applications are nowadays broadly available [1]. Filling the polymer resin with a powder material—followed by subsequent (post-) processing steps—even enables AM of ceramic or metal components [2–5].

The challenges in AM generally lie in reproducibility from part-to-part and print-job-to-print-job, productivity/speed of the printing process and size of printable components, i.e. scalability [6]. Adapting a specific process to an intended geometry and/or printer generally also implies a large portion of trial-and-error in tuning process parameters [7]. Naturally, manufacturers provide well documented resins accompanying their proprietary printer in an attempt to resolve part of this issue, but it does not entail a generic solution. A noteworthy path towards increased part quality in VP is the integration of sensors and (closed loop) control schemes into the printer [8–10].

The complexity of the VP process, in the context of the challenges addressed above, originates from the intrinsic multiphysical nature of the process [11,12]. Regardless of whether the printing system uses a bottom-up (constrained surface) or top-down irradiation (free surface)—as illustrated in Fig. 1 for a two-dimensional irradiation, Digital Light Processing (DLP), system—the VP process starts with the addition of a layer of resin of predefined thickness in the order of 50 μm. As soon as this so-called "recoating" step is completed, the photo-polymerization reaction is initiated by a UV projection of the cross-section of the product [13]. Absorption limits the light's penetration depth into the resin. In all locations where enough photons are available to be absorbed by the initiator, the liquid monomer polymerizes; a process which is accompanied by an exothermic temperature increase and chemical shrinkage [14]. As soon as a critical amount of energy, ϵ_c, is supplied, the conversion reaches a threshold and solidification occurs [15]. The accumulated effect of inhomogeneous shrinkage in the stack of layers that shape a component can cause deformation/warpage [16,17]. The number of relevant physical effects increases further when accounting for effects such as photobleaching [18–21] or the presence of inhibitor species such as oxygen [22–26].

The combination of these effects and their complex interplay makes accurate predictions of the quality of the printed component cumbersome. A simulation tool that captures the multiphysical nature of the AM process greatly enhances the process from design, material, printer and

* Corresponding author.
E-mail address: j.j.c.remmers@tue.nl (J.J.C. Remmers).

https://doi.org/10.1016/j.addma.2021.101922
Received 13 July 2020; Received in revised form 3 February 2021; Accepted 16 February 2021
Available online 3 March 2021

printing conditions towards a functional and qualitative part. Different authors have worked on modeling the printed part for both scanning laser (stereolithography) and full-field irradiation (mask projection or DLP) systems. Starting from Jacobs' cure depth model [15], in the following papers a rough distinction can be made between attempts that capture the effect of the layered nature of the AM process by applying selective shrinkage to a predefined geometry [16,27–30] or papers that incorporate highly detailed physics to predict the polymerized profile of a single or a limited number of layer(s) as a function of the UV light input [22,31–34]. The distinctive characteristic of the current work is that it predicts the printed/solidified geometry on a full-component scale—and the (unintended) deformation/warpage in it—through multi-physical modeling of irradiation, conversion, mechanical solidification and chemical shrinkage, with the sliced cross-sections of the target component as the departing point. This is accomplished by finite element simulation in an immersed setting, for which the model input is the applied irradiation pattern that corresponds to the (sliced) target geometry, analogous to previous work by the authors on VP for ceramics [11,12]. In contrast to those works, the scope of this work is restricted to the prediction of VP for an unfilled polymer, whilst including a qualitative validation for the DLP process.

In the following, first, the theoretical formulation of the framework will be addressed, after which the experimental approach to obtain validation samples will be introduced. Subsequently, the model parameter identification is presented. The work will be concluded by the validation of the developed simulation framework.

2. Modeling framework

The developed simulation framework is implemented in a dedicated finite element code tailored for simulating direct and indirect AM processes [35]. The general finite element formulation is considered outside the scope of this work, but the interested reader can find a plethora of relevant literature, e.g., [36,37]. Within this work, the framework is applied to a bottom-up VP approach (cf. Fig. 1), which is schematically depicted in Fig. 2. The repetitious process initiates with the build-plate moving upwards by (effectively) a layer thickness. Afterwards, patterned light from the projector enters the vat through the transparent slab, inducing the photopolymerization reaction. The description of the considered physics, i.e. irradiation, photopolymerization, the additive nature of the process and solidification—which rely on the model formulation published in a previous paper [12]—are addressed in the following Sections 2.1 to 2.4. Section 2.5 addresses relevant aspects regarding the numerical implementation. Effects related to the recoating step, either in a top-down or bottom-up system, are not accounted for and the (instantaneously) deposited layer is considered to be flat [38].

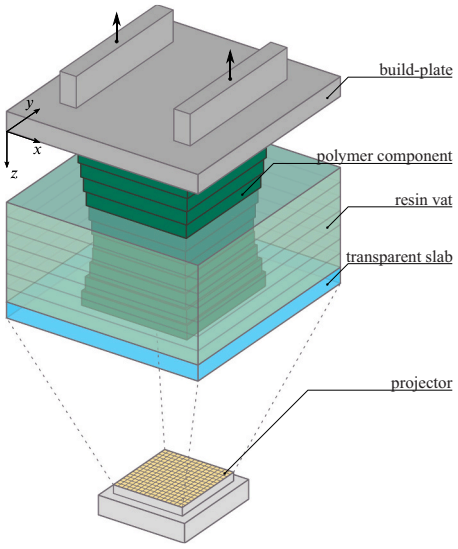

Fig. 2. Schematic visualization of the bottom-up DLP system considered within this work.

2.1. Illumination

Capturing the relevant physics starts with a suitable irradiation model for the DLP process at hand, which is based on the work of Kang

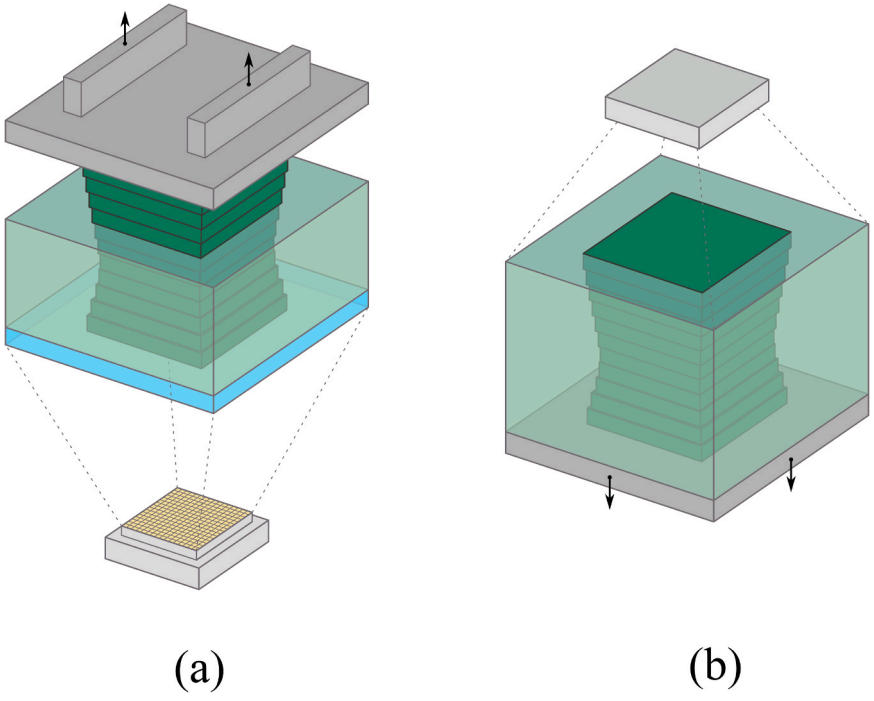

Fig. 1. Illustration of a typical bottom-up (a) and top-down (b) irradiation DLP system. Compared to the UV light source, the build-plate is located on the opposing side and the arrows denote its direction of motion.

et al. [34]. In contrast to direct laser illumination, as discussed in Ref. [12], the intensity profile of a single pixel is not a general two-dimensional Gaussian function; instead it reveals a rectangular cross section. The corresponding intensity distribution in a global coordinate system, $\vec{x} \in R^3 = (x,y,z)$, for a pixel i located at $\vec{x}_{S_i} = (x_{S_i}, y_{S_i}, z_{S_i})$, can be formulated as

$$I_{p,i}(\vec{x} - \vec{x}_{S_i}, t) = I_{p,i,\max}(t)\exp\left(-2\frac{[r(\vec{x} - \vec{x}_{S_i})]^2}{[w(\vec{x} - \vec{x}_{S_i})]^2} \right), \tag{1}$$

with $I_{p,i,\max}(t)$ the pixel's peak intensity in the horizontal center, i.e. $(x - x_{S_i}, y - y_{S_i}) = (0, 0)$, at time t. In this equation, $r(\vec{x} - \vec{x}_{S_i})$ and $w(\vec{x} - \vec{x}_{S_i})$ are given by

$$r(\vec{x} - \vec{x}_{S_i}) = \| \vec{x} - \vec{x}_{S_i} \|_2, \tag{2}$$

$$w(\vec{x} - \vec{x}_{S_i}) = w_0 \frac{r(\vec{x} - \vec{x}_{S_i})}{f_{sq}(\vec{x} - \vec{x}_{S_i})}, \tag{3}$$

where w_0 is the intensity distribution's $1/e^2$ Gaussian half-width and f_{sq} ensures the rectangular pixel shape through

$$f_{sq}(\vec{x} - \vec{x}_{S_i}) = \begin{cases} x - x_{S_i}, & \text{if } \left|\dfrac{y - y_{S_i}}{x - x_{S_i}}\right| \leq 1, \\ y - y_{S_i}, & \text{if } \left|\dfrac{y - y_{S_i}}{x - x_{S_i}}\right| > 1. \end{cases} \tag{4}$$

An example intensity profile of a single pixel is provided in Fig. 3. The corresponding total light source intensity profile is then provided by using the cumulative intensity as

$$I_0(\vec{x}, t) = \sum_i I_{p,i}(\vec{x} - \vec{x}_{S_i}, t). \tag{5}$$

The horizontal position of a pixel simply follows from the distance between the pixels, i.e. the pitch Π, as $x_{S_i} = \Pi(n_x - 1/2)$ and $y_{S_i} = \Pi(n_y - 1/2)$. In the latter, n_x and n_y are integers that vary between 1 and the number of pixels in x- and y-direction, respectively, N_x and N_y, i.e. $n_x = 1, 2, \ldots, N_x$ and $n_y = 1, 2, \ldots, N_y$. z_{S_i}, i.e. the out-of-plane position of pixel i, will be addressed later. The result for a 6×6 grid with 8 activated pixels (with characteristics equal to the one in Fig. 3, $w_0 = 50$ μm and $\Pi = 50$ μm) is shown in Fig. 4. Eq. (5) is implemented in the numerical framework as a two-dimensional field that is updated once for every unique layer's bitmap. This is not necessarily equivalent to the number of layers, because components with edges aligned with the z-direction can have the same cross-section across multiple layers. The ability of this individual pixel model to capture the cumulative effect in the physical process was proven by Kang et al. [34]. The interested reader may also find additional experimental support in the recent work of Emami and Rosen [39] that examines the effect of the light field in, e.g., the Gaussian beam's focus.

If we exploit that Beer-Lambert's law provides the in-depth light absorption in the z-direction, the three dimensional intensity profile in the material points (assuming perpendicular incidence) is provided by

$$I(\vec{x}, t) = \widetilde{I}_0(x, y, t)\exp\left(-(z_{S_i}(t) - z)/D_p \right) \tag{6}$$

with D_p the *penetration depth*, i.e. the depth where the irradiance has reduced to e^{-1} of the initial value [13,15] and z_{S_i} the z-coordinate where the light enters the material, such that $I(x, y, z_{S_i}, t) = I_0(x, y, t)$, which depends on the number of layers and the layer thickness δ, cf. Fig. 2. $\widetilde{I}_0(x, y, t)$ in Eq. (6) is the result of a linear interpolation step on the (sufficiently refined, but discrete) field I_0, which ensures that the x- and y-coordinates where the two-dimensional intensity profile I_0 is stored do not necessarily need to coincide with the (x, y)-coordinate of the material/integration points.

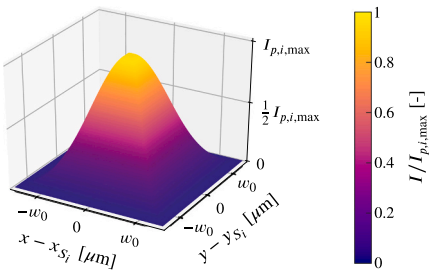

Fig. 3. Intensity profile for a single pixel $I_{p,i}(x_i, y_j)$. The depicted irradiance distribution is normalized by $I_{p,i,\max}$.

2.2. Photopolymerization

Different highly sophisticated models exist in literature to capture the physics of photopolymerization in detail [18–22,31,33,34,40,41]. For the solidification process, the conversion from monomers to a long-chained polymer is of interest. The conversion process is however influenced by multiple factors that can be accounted for. In a traditional mechanistic form for free radical photopolymerization, one can account for the rate of propagation and termination of the monomer consumption, k_p and k_t, respectively, and the influence of temperature therein [42], i.e.

$$-\frac{d[M]}{dt} = k_p[M]\left(\frac{\psi I_a}{k_t}\right)^{1/2}. \tag{7}$$

$[M]$ in the above equation is the monomer concentration, I_a is the absorbed intensity and ψ the quantum yield for initiation. The differential equation in Eq. (7) is completed by an initial condition $[M](0) = [M]_0$. Typically, the progress of the polymerization reaction is quantified by the degree of conversion p:

$$p = \frac{[M]_0 - [M]}{[M]_0} = 1 - \frac{[M]}{[M]_0}. \tag{8}$$

Extensions might incorporate more species balances [18–21], the diffusion of species through the resin, or the presence of inhibitor species [22,43].

To reduce the number of model parameters, this work applies a phenomenological conversion law accompanied by a simple mathematical formulation that accounts for oxygen inhibition. The latter is introduced to capture the limited *print-through*—which is the additional (unintended) solidification in layers before the one currently irradiated—encountered in printed specimens.

The phenomenological monomer evolution can be formulated in a similar form compared to Eq. (7), i.e.

$$-\frac{d[M]}{dt} = \mathscr{P}[M]\sqrt{I}, \tag{9}$$

with $\mathscr{P}$ a constant rate of polymerization. This simplified first-order reaction equation is shown to capture the photopolymerization process accurately [8], although second-order reactions are reported in literature as well [42].

Considering that our interest lies in the degree of conversion and not in the evolution of the monomer concentration, the normalized quantity $m = [M]/[M]_0$ is introduced instead. Substituting m into Eqs. (9) and (8) provides

$$-\frac{dm}{dt} = \mathscr{P}m\sqrt{I}, \tag{10}$$

$$p = 1 - m, \tag{11}$$

for which $m(t = 0) = m_0 = 1$. This model assumes that eventually all

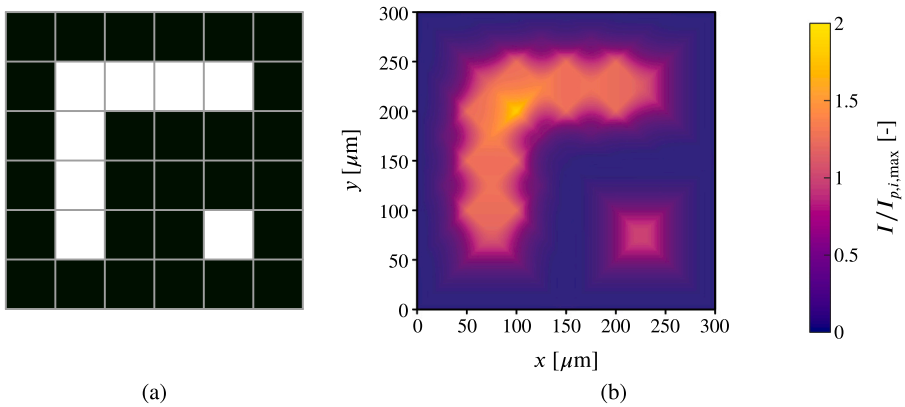

Fig. 4. Illustration of the accumulative effect of neighboring (activated) pixels for the pixel characteristics shown in Fig. 3, $w_0 = 50$ μm and $\Pi = 50$ μm. The activated pixels are shown in (a) and the resulting irradiance distribution is shown in (b). Note that the maximum intensity magnitude is larger than $I_{p,i,\max}$, which is used as a normalization value.

monomer is turned into polymer whereby the conversion reaches one. In practice, after vitrification occurs, the mobility of the non-reacted species decreases and p reaches a plateau value < 1 [2,8,24,44]. To account for this, Eq. (11) is pre-multiplied by an asymptote accounting for the degree maximum of conversion, $p_\infty < 1$, such that the absolute conversion reads

$$\widehat{p} = p_\infty(1 - m) \tag{12}$$

In the majority of literature considering VP—instead of accounting for the evolution of the monomer conversion—a relation is identified between the energy input into the resin and the so-called *cure depth* C_d. For a single source intensity magnitude, a number of different irradiation times is used to characterize the relationship between exposure ϵ and C_d. The relationship between the natural logarithm of exposure, $\ln(\epsilon)$, and C_d is typically found to be linear [15,43,45]. The corresponding slope is defined as the penetration depth D_p, i.e. the same parameter as introduced in Eq. (6). The intersection with a C_d of zero is the so-called *critical exposure* ϵ_c [13]. To relate the resulting *working curve*, i.e. $C_d(\epsilon)$—and in particular the critical exposure—to Eqs. (10) and (11), it is key to note that after exposure of the resin with ϵ_c, gelation occurs and solidification initiates. In the framework of polymerization, this tipping point is generally termed the *gel point*, i.e. p_{gel} [15].

The working curve has proven to be a valuable tool for characterizing resins in VP and for tailoring process parameters to improve printing quality. It is, however, derived from a single resin exposure. Consequently, in a multi-layer process, it does not capture the extent of the solidification accurately, or, to put this more clearly: relying only on the exposure in a material point, a large amount of (non-existent) print-through would be predicted. To overcome this limitation, different researchers make use of (partial) differential equations to accurately capture the cure evolution [22,25,26,41,46]—even while only considering a single irradiation step, i.e. the conversion of a single layer. Usually, the limiting factor is attributed to the inhibition of oxygen. A more phenomenological approach to capture this effect is used in the work of Kang et al. [34], who experimentally identified a critical intensity based on the irradiation time that follows a relationship of the form $I_c = a\ln(t/1[s]) + b$, where a is found to be < 0 and b is the intensity threshold at $t = 1$ s. The critical intensity acts as a threshold value; if a certain exposure is applied in a specific time interval, then the intensity should at least be I_c to support solidification. For the time-continuous modeling framework in this work, we invert this logarithmic relationship, giving an inhibition induced time delay:

$$\tau_d = \exp\left(\frac{\imath_c - I(\vec{x})}{\imath_s}\right), \tag{13}$$

where $\imath_c$ and $\imath_s$ are two resin/process constants with the unit of intensity. The purpose of Eq. (13) is to postpone the initiation of the conversion process, by enforcing $d[M]/dt = 0$ while $t < \tau_d$. Note that the phenomenon of a time delay as described by Eq. (13) is also observed experimentally [8,9].

2.3. Capturing the additive nature

In simulating an additive process, the size of the computational domain continuously increases. To circumvent the associated bookkeeping required, the most common methods for AM simulations perform a pre-meshing of the target printed geometry. Imitating the additive nature of the process is typically done using an element activation technique [47,48].

In this work, the outcome/resulting geometry is not assumed a priori, but follows from the process simulation instead—through the input irradiation. A section of the (resin) vat, inside which the part fits, is defined as the computational domain. New elements are added, one layer at a time, before moving to the next irradiation step.

This procedure may seem similar to the aforementioned conventional pre-meshing of the target geometry, but this only partly true. Highly similar is that the nodes of the newly added elements are placed at the coordinates where they were 'intended' in the predetermined computational domain, i.e. the vat section, which can be done conveniently since the finite element mesh is of a voxel type. The major difference lies in the applied immersed setting, which allows updating the contour of the emerging solidified geometry.

2.4. Evolution of the mechanical properties

The modeling framework accounts for two aspects affecting the evolution of mechanical properties. These are *(i)* the shrinkage that is associated with the polymerization and *(ii)* the progression of the (solid-like) material's properties during solidification. The influence of temperature is neglected while considering the above aspects in combination with an elastic constitutive behavior, i.e. the process is assumed isothermal. This simplification is made since it is the final printed state that is of interest here (with a homogeneous temperature throughout the component). Only a limited influence of thermal expansion during the irradiation step is expected.

Whereas the physics in Sections 2.1 and 2.2 can be solved inside a material point using the source and initial conditions, for the mechanics, a balance equation has to be solved on the entire computational domain. The linear momentum balance, omitting dynamic effects, i.e. assuming a quasi-static process, is formulated as

$$\vec{\nabla}\cdot\boldsymbol{\sigma}(\vec{x}) + \rho\,\vec{b} = \vec{0}, \tag{14}$$

where $\boldsymbol{\sigma}$ is the stress tensor, $\vec{b}$ is the gravitational (body) force vector per unit volume and ρ the mass density. Strains enter Eq. (14) through the constitutive equation, which, in this work, is given by Hooke's law:

$$\boldsymbol{\sigma}(\vec{x}) = {}^4\boldsymbol{C}(\vec{x}) : \boldsymbol{\varepsilon}_e(\vec{x}), \tag{15}$$

with ${}^4\boldsymbol{C}$ the fourth-order elastic stiffness tensor and $\boldsymbol{\varepsilon}_e$ is the elastic strain tensor.

The total strain consists of the combination of the elastic strain $\boldsymbol{\varepsilon}_e$ and the polymerization shrinkage strain $\boldsymbol{\varepsilon}_{ch}$, i.e.

$$\boldsymbol{\varepsilon}(\vec{x}) = \boldsymbol{\varepsilon}_e(\vec{x}) + \boldsymbol{\varepsilon}_{ch}(\vec{x}). \tag{16}$$

$\boldsymbol{\varepsilon}_{ch}$ is linearly dependent on the conversion via

$$\boldsymbol{\varepsilon}_{ch}(\vec{x}) = \frac{1}{p_\infty}\hat{p}(\vec{x})\varepsilon_{ch,max}\boldsymbol{I}, \tag{17}$$

in which $\varepsilon_{ch,max}$ is the strain at maximum conversion p_∞ and $\boldsymbol{I}$ the unity tensor to account for the volumetric shrinkage. Note that Eq. (17) is simply obtained from the semi-analytical volumetric shrinkage strain [29,49,50]. If needed, Eq. (16) can be further extended with e.g. thermal, viscous and plastic strains.

Using a finite element discretization, the total strain needs some additional considerations. Upon generation of a new layer of material—with its corresponding new nodes at the intended positions, and pre-existing nodes from the previous layer in a deformed configuration, cf. Section 2.3—an initial strain already exists. This prior strain, present in the element upon introduction, should not induce any stress and is therefore extracted from the (current) element's strain (inside the integration points) to obtain the total stain, i.e.

$$\boldsymbol{\varepsilon}(\vec{x}) = \boldsymbol{\varepsilon}^{el}(\vec{x}) - \boldsymbol{\varepsilon}_0^{el}(\vec{x}), \tag{18}$$

which is next substituted in Eq. (16).

The second aspect of the evolution affects Eq. (15) through the stiffness tensor ${}^4\boldsymbol{C}$. The isotropic linear elastic formulation of ${}^4\boldsymbol{C}$ is a function of the Poisson's ratio ν and the Young's modulus E. To capture the solidification, the Young's modulus is defined conversion dependent:

$$E(\hat{p}) = \left\{ \begin{array}{ll} e_0 E_{pol} & \text{for} \hat{p} < p_{gel}, \\ \left(\dfrac{1-e_0}{p_\infty - p_{gel}}(\hat{p} - p_{gel}) + e_0\right) E_{pol} & \text{for} \hat{p} \geq p_{gel}. \end{array} \right\} \tag{19}$$

This bilinear function uses a lower bound for E, for conversion $< p_{gel}$, which is much smaller than the polymerized Young's modulus E_{pol} by multiplication with $e_0 \ll 1$. Once the gel point is reached, the Young's modulus linearly increases from $e_0\, E_{pol}$ to E_{pol} at maximum conversion p_∞. Technically, in the fluid phase the resin's E is not defined, but—since the interest lies in the solidification—a value close to zero suffices and facilitates the (immersed) finite element simulation. The resulting stiffness matrix is isotropic and the Poisson's ratio is assumed constant. An equivalent linear dependence of the stiffness on the conversion (through exposure and reaction kinetics) is also found experimentally [51,52].

2.5. Numerical implementation

The mechanical description in Section 2.4 is completed by appropriate boundary conditions: at $z = 0$ the displacements of the nodes are fully constrained to account for a proper bonding with the build-plate. Because the simulation only considers a section of the (resin) vat, the lateral boundaries of the domain are allowed to contract freely. The separation force related to bottom-up VP systems—associated with detachment from the transparent slab, cf. Fig. 2—is not accounted for.

The section of the resin vat of interest, i.e. the rectangular prism around the immersed component, is discretized using cube-shaped linear hexahedron (8-node) finite-elements of uniform size. Numerical integration is performed using Gaussian quadrature. Within the current formulation, the conversion equation is solved through a simple ordinary differential equation inside the integration points using the local light intensity as input. An iterative GMRES solver is used to derive the momentum equilibrium of Eq. (14) and time-steps are uniform, i.e. $\Delta t = 0.05$ s. Upon placement of a new layer, the degree of conversion $\hat{p} = 0$ and the initial strain $\boldsymbol{\varepsilon}(\vec{x}) = 0$ in each integration of each element, through Eq. (18).

3. Experimental setup

The modeling framework is qualitatively validated through a geometrical correlation with physically printed samples. The following Sections 3.1 and 3.2 address the experimental approach and the (intention of the) printed geometries, respectively.

3.1. Process characterization

In order to perform the validation step, a number of sample geometries are printed on a Rapidshape S60 mini DLP printer, which was schematically depicted in Fig. 2. The pixels' pitch Π is approximately 48 μm and layers are printed with a thickness $\delta = 50$ μm (which are self-corrected with $+ / - 10$ μm accuracy).

Samples are printed with a prototyping material containing multiple methacrylates, 2 wt% photo-initiator Irgacure 819 and 0017 wt% of a blue light-blocking dye. The corresponding working curve parameters are a critical exposure ϵ_c of 11 mJ/cm^2 and a penetration depth D_p of 117 μm. The geometries are not additionally reinforced by support structures during printing. To ensure sufficient bonding with the base plate, the first three layers are printed with an exposure of $\epsilon_0 = 100$mJ/cm^2, while the exposure for the remaining layers is $\epsilon_1 = 18$mJ/cm^2.

After printing, the samples are removed from the base plate using a glass scraper and cleaned (twice) using IPA in an ultrasonic cleaner. The samples are not post-cured, in line with the numerical simulations.

To extract the full three-dimensional geometrical shape of the printed samples, an industrial μCT scanner (Phoenix Nanotom) is used. The samples are attached to a rod—on which the sample rotates for imaging purposes—at the build-plate-cut-plane using a small amount of clay material. Using the clay, the samples are placed at an angle to optimize the visualization, but the clay can leave traces in the processed geometries. Although multiple samples are printed of each geometry, see Section 3.2, only two are examined. From the resulting three-dimensional voxelized data, obtained with a resolution of 4 μm, the outside contours are extracted in an stl-format—after removal of the air and rod/clay (by thresholding using VGSTUDIOMAX software, version 1.0)—to conveniently compare to the numerically obtained data. Using these (relatively) high resolution images allows to assess the solidified contour of individual layers and the presence of small scale defects.

3.2. Components' geometry specification

Three different sample categories are printed, all of size ≤ 3 mm. The design of these will be introduced—and compared to the actually printed samples—in Sections 3.2.1 to 3.2.3. An additional simple brick like shape ($5 \times 4 \times 3$ mm^3) is printed for characterization of the mechanical properties by indentation experiments.

3.2.1. Pixel characterization

The first sample, displayed in Fig. 5, is tailored to identify the irradiation characteristics of the system. It consists of a rectangular base ($1750 \times 1750 \times 500$ μm^3) that has its lateral faces aligned with the x-,

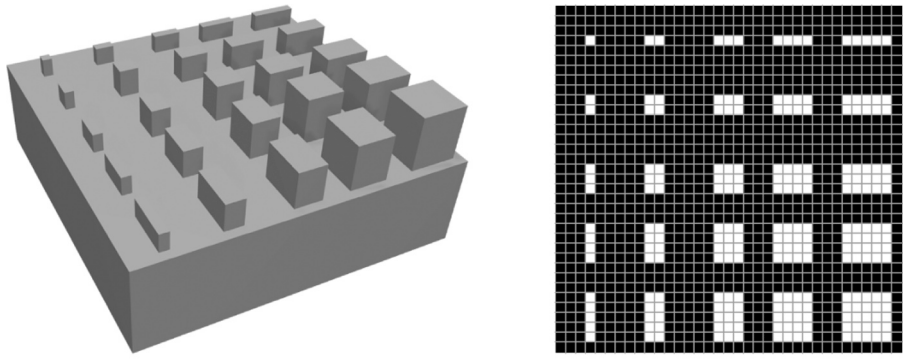

(a) (b)

Fig. 5. Visualization of the irradiation characterization sample. Total dimensions of the part are 1750 × 1750 × 800 μm^3 and all features are coinciding with a 50 μm interval grid in *x*-, *y*- and *z*-direction. A perspective view is shown in (a) and an *xy*-plane, just above the base ($z = 500$ μm), is depicted with the grid in (b).

y- and *z*-direction of the printer, with simple characterizing features on top. The smallest features are two layers high ($2\delta = 100$ μm) with a dimension of 50 μm in the horizontal plane. The dimensions of the square shapes on the diagonal from the top-left to the bottom-right equal 50, 100, 150, 200 and 250 μm. From small, to large, the height of these shapes increases by a single layer-thickness δ. The remaining shapes have the same dimensional length, width and height as the (smallest) in-line (w.r.t. the *x*- and *y*-axis) shape on the (from the top-left to the bottom-right) diagonal. Due to the pitch between pixels, the shapes are expected to consist of one to five pixels in a row. Considering the printed sample will always be the result of the multi-physical process, the thickness of the base is chosen thick enough to ensure that shrinkage and (resulting) deformation have minimal influence.

Two of the printed geometries are displayed in Fig. 6. The samples show the widened first three layers as a result of the increased energy input and a repetitive pattern in both vertical and horizontal directions, induced by the layers and individual pixels, respectively. Minor variations between the samples exist which are introduced by—but definitely not limited to—minor differences in the sliced cross-sections (as can be deduced from Fig. 6b) and inhomogeneities in the intensity profile from the mercury-vapor lamp in the DLP system, for different positions on the print bed, and the cleaning process.

When comparing the target geometry (Fig. 5) to the actually printed ones (Fig. 6) a significant deviation becomes clear. The most obvious differences are the rounded shape of the edges of both the sample's base and pillars and the fact that a single (row of) pixel(s) is insufficient to ensure solidification. For the 100 × 100 μm^2 (2 × 2 pixels) square pillar only hardly distinguishable features remain. This illustrates the profound influence of the pixel characteristics—and the knowledge thereof—for the fabrication of fine featured components.

3.2.2. T-shape

The second geometry allows to identify the warpage in a free-standing overhang, to tailor the predicted print-through in the model. Different sizes are printed, as shown in Fig. 7, with the corresponding (target) dimensions specified in Table 1. Note that the different samples are symmetric around the central vertical axis, which motivates the *T* naming convention. The pedestal is added to ensure proper bonding to the base plate of the printer.

The result after slicing, printing and cleaning is shown in Fig. 8. Whereas in the intended samples the faces are flat and the corners sharp, cf. Fig. 7, this is no longer the case for the printed samples. Even though some curvature can be recognized in the top section of the T, the amount of warpage is rather limited. Furthermore, based on the absence of surplus thickness in the overhang, the amount of print-through appears small. These findings should be confirmed in the modeling approach in Section 4.

3.2.3. H-shape

The final sample category is shaped in the form of an *H* on a pedestal, as shown in Fig. 9. Sample dimensions are provided in Table 2. This geometry is based on an H-shaped diagnostic sample which is frequently used to benchmark the accuracy of an SLA system [53–56]. However, in comparison, the currently printed H-samples are smaller in size and include a sloped overhang. As a result, they do not require any support structures. The addition of a pedestal ensures proper bonding to the build-plate for the smaller sample(s).

The H-samples were fabricated to quantify a number of interesting phenomena in the VP process [53], which are also shown by the printed samples. This is illustrated in Fig. 10, which depicts the three-dimensional scanned geometries and a cross-section through the

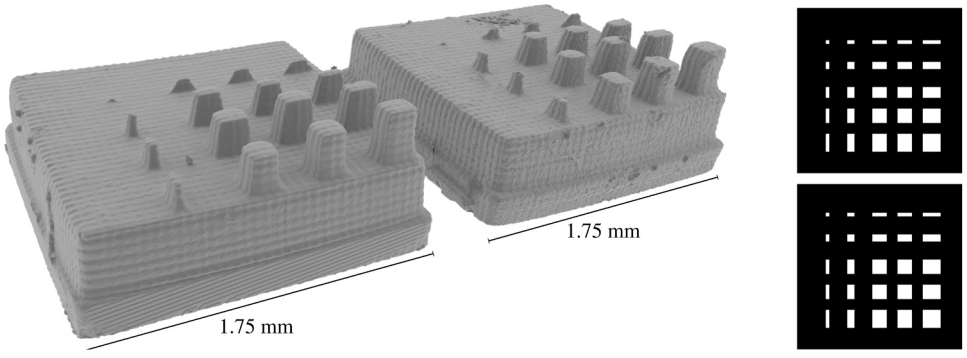

(a) (b)

Fig. 6. The geometry of two printed samples, as obtained from CT imaging. A perspective view is shown in (a) and the corresponding bitmap (input geometry), for the left (top) and right (bottom) component, at the *xy*-plane just above the base are depicted in (b).

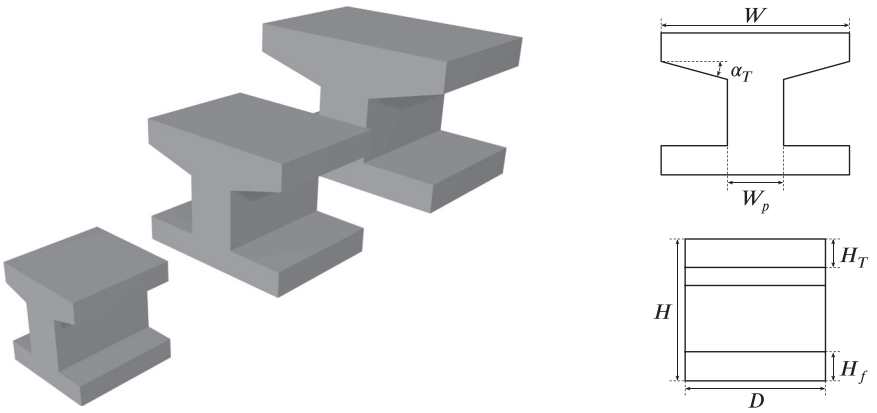

Fig. 7. Geometry of the target T_{1-3}-samples in (a) with the dimensions in front- and side-view in (b). Values for the dimensions are provided in Table 1.

Table 1
T-sample dimensions as depicted in Fig. 7b.

	W (μm)	W_p (μm)	H (μm)	H_T (μm)	H_f (μm)	D (μm)	α_T (°)
T_1	1000	400	1000	200	200	1000	15
T_2	2000	600	1500	300	300	1500	15
T_3	3000	800	2000	400	400	2000	15

middle of the part. The cross sectional contours in Fig. 10b are incorporated to illustrate that all samples show a particular deformation pattern. Firstly, the cross-sectional width of the part is more narrow in the horizontally connected regions, i.e. near the base and the overhang, compared to in the pillar sections. Furthermore, the top pillars seem to warp outwards—an effect that is most dominant starting from the overhang, which is referred to as a waist distortion [53]. Whereas the overall contour of the part is fairly smooth, indicating sufficient cure, the overhang section is jagged. This illustrates the print-through effect and demonstrates that the cleaning process can have a significant influence on the resulting thickness of overhang regions, when there is no sharp gradient in the conversion profile [23].

4. Parameter characterization

In the following Sections 4.1 and 4.2, first, the conversion parameters are characterized, followed by identification of the solidification characteristics. The optimized parameter set introduced below is obtained through a sensitivity analysis. Even though a subdivision in parameter categories is used, it is key to note that the simulation results are the lumped effect of all the chemo-mechanical model parameters. It should be noted that the contour of the resulting printed component is also dependent on the cleaning process. Throughout the remainder of this paper it is assumed that a degree of conversion of at least p_{gel} is sufficient to withstand cleaning. Simulation results are obtained with 3 cube elements per layer thickness while the intensity interpolation grid points are spaced 5 μm apart and applied exposures are equal to the values denoted in Section 3.1. Only the sample in Fig. 5 and the smallest samples in Figs. 7 and 9, i.e. T_1 and H_1, are used for the parameter identification.

4.1. Conversion characteristics

The pixel characterization sample introduced in Section 3.2.1 is tailored to identify irradiation characteristics. For the input intensity a

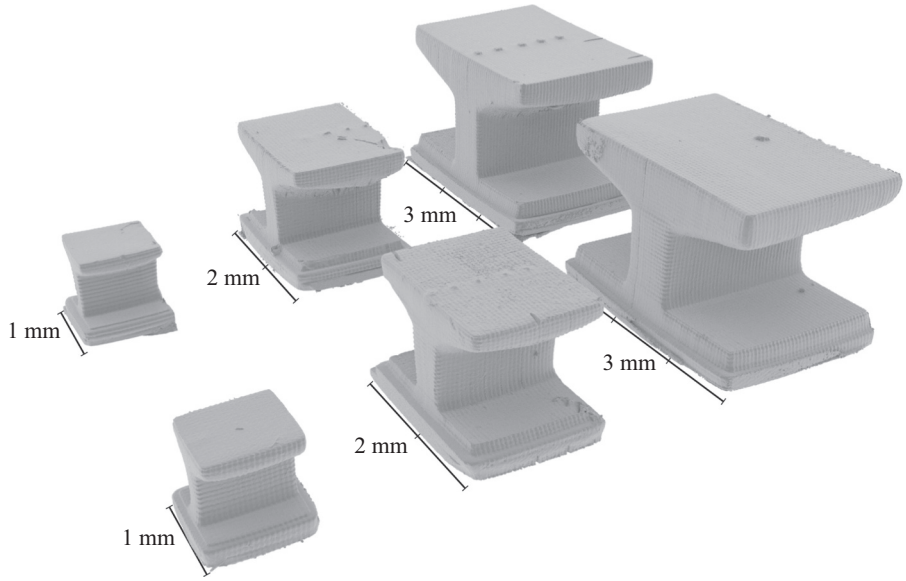

Fig. 8. Geometry of the printed T_{1-3}-samples with different sizes, i.e. 1, 2 and 3 mm width, two of each.

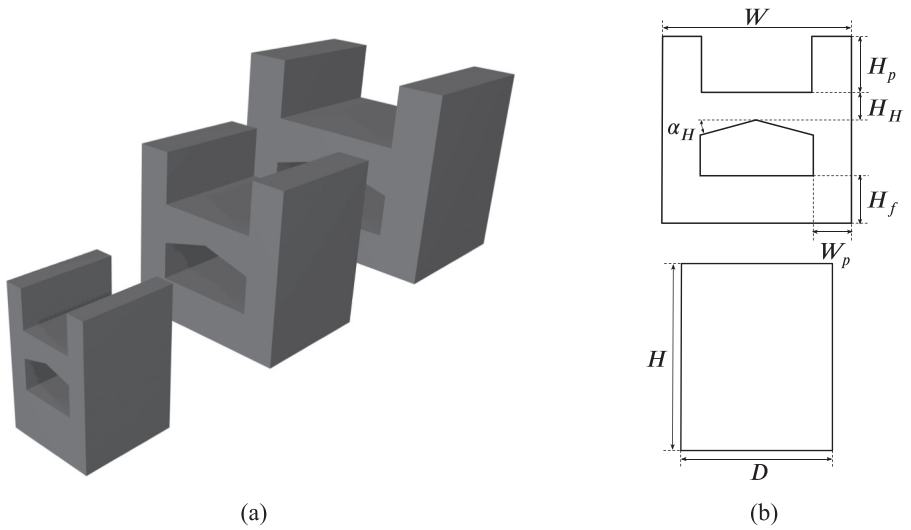

Fig. 9. Geometry of the target H_{1-3}-samples in (a) with the dimensions in front- and side-view in (b). Values for the dimensions are provided in Table 2.

Table 2
H-sample dimensions as depicted in Fig. 9b.

	W (μm)	W_p (μm)	H (μm)	H_H (μm)	H_p (μm)	H_f (μm)	D (μm)	α_H (°)
H_1	1000	200	1500	200	400	500	1000	15
H_2	2000	400	2000	300	600	500	1500	15
H_3	3000	600	2500	400	800	500	2000	15

representative value of $I_0 = 100\text{W}/\text{m}^2$ is chosen [43], which, combined with a specific irradiation time provides the critical exposure. Specification of a representative value for intensity is deemed appropriate because its effect on the resulting component is found limited. Process parameters that have a profound influence are the pixel properties, i.e. $I_{p,i,\max}$ and w_0 in Eqs. (1) to (3). Together with the conversion parameters, $\mathscr{P}$, $\imath_c$ and $\imath_s$, they govern the volume that solidifies.

The optimal combination of these parameters is found as $I_{p,i,\max} = 32\text{W}/\text{m}^2$, $\mathscr{P} = 3{\cdot}10^{-2}\text{m s}^{-1}\text{W}^{-\frac{1}{2}}$, $\imath_c = 50\text{W}/\text{m}^2$ and $\imath_s = 20\text{W}/\text{m}^2$. w_0 follows from the combination of $I_{p,i,\max}$ and the (average) plateau value that provides I_0—for a sufficiently large grid of pixels, i.e. in this case 50×50 using $\Pi = 48$ μm—resulting in $w_0 = 59.91$ μm. The conversion rate $\mathscr{P}$ follows directly from the critical energy. The provided value of $\mathscr{P}$ ensures that $\widehat{p} = p_{\text{gel}}$ is reached after applying the critical exposure ϵ_c whilst accounting for $p_\infty = 0.7$, which will be addressed in Section 4.2.

Both the simulation result and the resulting printed pixel characterization sample are displayed in Fig. 11 for the two sets of input bitmap slices displayed in Fig. 6b. Note that the depicted simulation results show the (deformed) volume with $\widehat{p} > p_{\text{gel}} = 0.2$. The absolute distance between the CT-scanned sample and the simulated geometry—extracted using the open-source software CloudCompare [57]—is included by color grading, revealing that the difference for the majority of the data points remains well below 25 μm. Fig. 11 indicates the relevance of the irradiance characteristics. Even though features of $1 \times n$ are irradiated, no (remaining) solidification occurs. On the other hand, the smallest irradiation surface that provides a distinguishable feature on the resulting print is the 2×2 area. Even though it results in a minimal protrusion, the simulation framework is capable of capturing it. It should be noted that in addition to the protrusion also a number of free-floating volumes are predicted by the simulation framework on top of the $2 \times n$ features. These are not accounted for in the absolute difference comparison, since these would not endure the extraction/washing process. For the printed pillars—and the contour of the base as well—the simulation result under-predicts the widening effect from top to bottom, but this effect is limited and therefore considered acceptable. Note that, unlike the printed samples, the simulated samples are still rigidly connected to the build-plate. Due to the linear-elastic

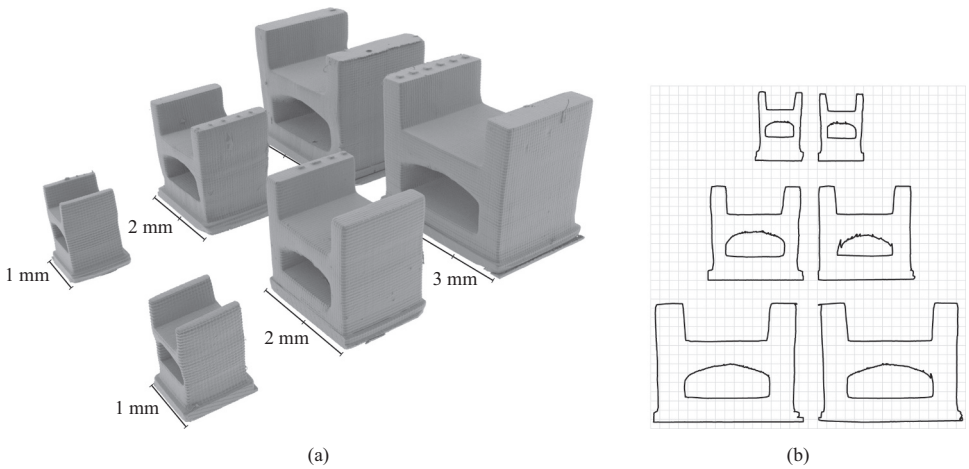

Fig. 10. Geometry of the printed H_{1-3}-samples in different sizes, i.e. 1, 2 and 3 mm width, two of each are shown in (a). In (b) the middle cross section is displayed on top of a (n arbitrary) square grid for all samples in (a), to better illustrate the deformation.

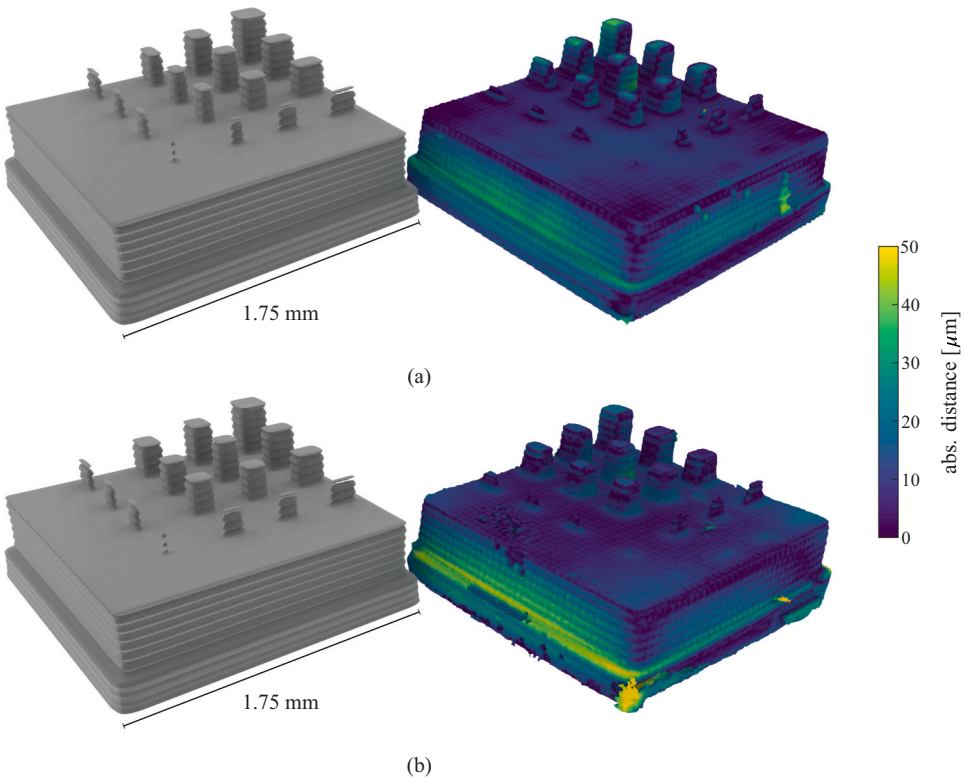

Fig. 11. Comparison of the simulated geometries for the pixel identification sample with the CT-scanned sample for the identified model parameters. Graphs (a) and (b) show two different simulations with the input bitmap of the corresponding printed sample, as indicated in Fig. 6b. Gray image (left) is the simulation result. The colored image (right) illustrates the absolute difference (in μm) between the printed sample and the simulated sample. The range of the color bar is limited to 50 μm. (For interpretation of the references to color in this figure legend, the reader is referred to the web version of this article.)

material model and the increased energy dose in the first three layers, with the corresponding higher amount of shrinkage, a build-plate release would induce an unrealistic concave deformation pattern of the sample as a whole. Indeed, the first three layers will be subjected to inelastic strains more significantly. The bottom of the printed samples is also relatively flat because these are cut from the base plate and no subsequent post-curing is applied.

The T-sample in Fig. 7 is ideal for identification of the print-through effect. Ideally, the amount of print-through would follow from the experimentally determined working curve, specifically through D_p. In addition, here τ_d, i.e. Eq. (13), is required to obtain the correct resulting solidified component's geometry (after washing). The resulting sample

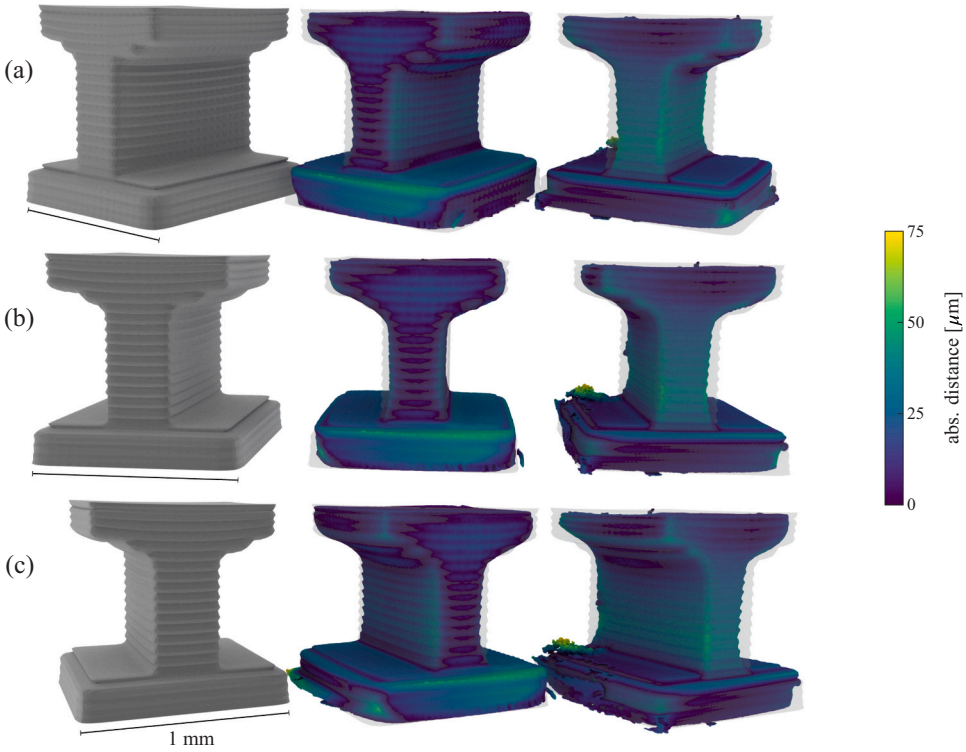

Fig. 12. Comparison of the simulated geometry for the small T-shape with the CT-scanned sample for the identified model parameters from three different angles, in (a)–(c). Gray image (left) is the simulation result, colored images (other two) illustrate the absolute distance (in μm) from the printed samples to the simulated sample. The range of the color bar is limited to 75 μm. For visual comparison, the CT images also include a transparent simulation geometry. (For interpretation of the references to color in this figure legend, the reader is referred to the web version of this article.)

geometries are shown in Fig. 12. The (absolute) difference between two printed samples and the simulation result is again indicated by the coloring of the printed samples, this time for three different views as depicted in Fig. 12a–c, respectively. The two dimensional representation is not ideal, but in the following only a single view is presented. In Fig. 12 a significant difference is noticeable between the two (right-hand side) printed samples. This is a clear indication of the limited reproducibility in the AM process, presumably caused by a local area of reduced intensity in the projection. The absolute difference between the predicted and the printed samples—with exception of some excess material on the pedestal—is less than a layer thickness for both samples. Even though the two depicted samples may appear limited considering reproducibility, the remainder of the printed samples are fabricated using the same settings—even in the same print-job. It should be noted, however, that capturing reproducibility does not fall within the scope of the model. An interesting observation is that the simulated result shows an influence of the geometrical slicing in the angled overhang, but in the printed samples this effect is hardly noticeable. In line with the printed results—even though the numerical resolution may be considered limited on the layer scale—the prediction also shows the components' gridded surface that demonstrates the influence of individual pixels.

4.2. Mechanical properties

Two different samples are of interest for the mechanical model description, i.e. the brick like sample and the smallest H-sample in Fig. 9. Of these, the former provides the Young's modulus at an assumed Poisson's ratio and the latter is used to determine the resin's shrinkage.

Indentation experiments on the brick-like sample for indentation depths ranging from 5 to 10 μm do provide a consistent Young's modulus of $E \approx 1$ GPa (with $\nu = 0.4$) for an exposure of ϵ_1. This is reflected by the simulation framework through the incorporation of an equivalent value for E at the conversion corresponding to ϵ_1, i.e. ≈ 0.5. Using $p_\infty = 0.7$, the Young's modulus at maximum conversion is chosen as $E_{\text{pol}} = 1.7$ GPa. The corresponding Poisson's ratio is $\nu = 0.4$.

The shrinkage strain is identified by comparing the deformation of the simulated H-sample to that of the printed ones, giving $\epsilon_{\text{ch,max}} = -0.05$, which is representative for an acrylic resin [29]. This maximum shrinkage strain holds for the conversion asymptote p_∞, which has been chosen at 70% conversion to capture the physical process limit [2,8,24,43,44,58] and, to a lesser extent, to limit the inhomogeneity of shrinkage within the sample, i.e. within a single layer and considering the different input exposures ϵ_0 (first 3 layers) and ϵ_1 (other layers). To account for the gravitational body force, i.e. $\vec{b} = (0, 0, 9.8)$ m/s^2—even though the significance is small at the length scale of the considered samples—the mass density of the medium, ρ, is assumed constant throughout the conversion and equal to 1150 kg/m^3.

The simulation result is visualized in Fig. 13 and shows remarkable correspondence with the printed samples. Yet, there are also some notable differences. Even though the widening of the first three layers is correctly captured, the printed samples show a larger shrinkage in the pedestal. For the printed samples, this difference appears more pronounced for the sides aligned with the 'geometrically-extruded' direction. This effect might therefore be induced while printing the remainder of the structure, i.e. the pillars and overhang. The outward directed warpage of the top pillars and the waist of the H-sample is captured accurately, but the total height of the printed samples is roughly a layer thickness less, compared to the simulated result. Note that the printed geometries—except for a small part of the pedestal and the overhang section—do not show a variation larger than that, i.e. < 50 μm.

5. Model validation

A total of three differently sized T- and H-samples are printed and analyzed, as addressed in Section 3. The two larger samples, with a width equal to two and three times that of the small sample (cf. Tables 1 and 2) are considered for model validation, i.e. to identify whether the size dependence can be captured accurately. The parameter set identified in Section 4 is used for this purpose. The largest samples (T_3/H_3) are simulated with a reduced resolution, i.e. 2 cube elements over the layer thickness.

5.1. T-shaped sample

The results for the T-shaped samples are depicted in Figs. 14 and 15 for the 2 and 3 mm wide sample, i.e. T_2 and T_3, respectively. In addition to the comparison of the simulated result to the printed result (top row), the difference between the target geometry—which is used for the sliced input into the DLP printer—and the printed sample is now also included (bottom row). For the T_2 sample, Fig. 14, the simulated geometry clearly matches the printed results quite accurately. The most dominant deviation is present in the overhang section. The difference of the target geometry with the printed samples (experimental deviation) is much more pronounced. For the larger T_3 sample, printing induced geometrical errors become less pronounced. Judging from the shape—including the rounded edges, pedestal broadening and reduction of the pillar width—the simulation does provide an accurate prediction of the resulting geometry. A significant deformation, which is not present in the printed samples, is however predicted in the overhang inducing narrow end-sections at the edges of the horizontal T-section. This indicates a restriction of the modeling framework in that it does not capture, e.g., the contact with the transparent slab, cf. Fig. 2. The differences between the target, predicted and printed samples for the two different sample sizes also indicate that the relevance of (geometry) predictive models in AM is more pronounced when printing samples/features closer to the resolution of the printer.

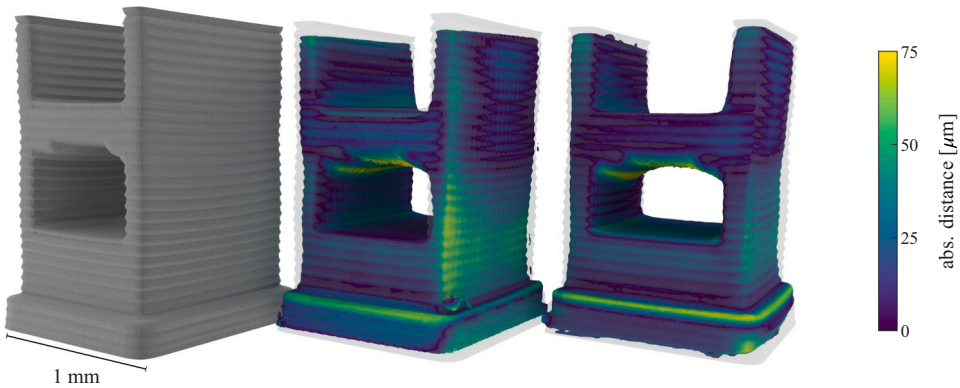

Fig. 13. Comparison of the simulated geometry for the small H-shape with the CT-scanned sample for the identified model parameters. Gray image (left) is the simulation result, colored images (other two) illustrate the absolute distance (in μm) from the printed sample to the simulated sample. The range of the color bar is limited to 50 μm. For visual comparison, the CT images also include a transparent simulation geometry. (For interpretation of the references to color in this figure legend, the reader is referred to the web version of this article.)

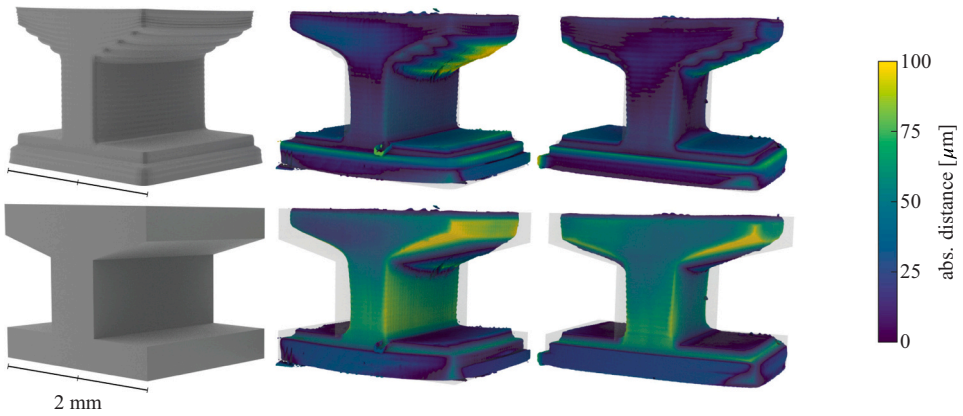

Fig. 14. Comparison of the simulated geometry with the printed samples (top row) and the target geometry with the printed samples (bottom row) for the T_2-shape. The range of the color bar is limited to 75 μm. For visual comparison, the CT images also include a transparent simulation/target geometry. (For interpretation of the references to color in this figure legend, the reader is referred to the web version of this article.)

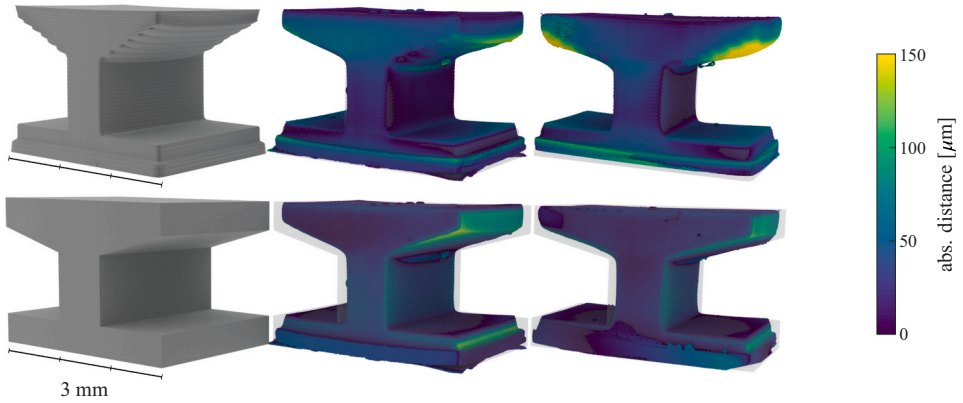

Fig. 15. Comparison of the simulated geometry with the printed samples (top row) and the target geometry with the printed samples (bottom row) for the T_3-shape. The range of the color bar is limited to 150 μm. For visual comparison, the CT images also include a transparent simulation/target geometry. (For interpretation of the references to color in this figure legend, the reader is referred to the web version of this article.)

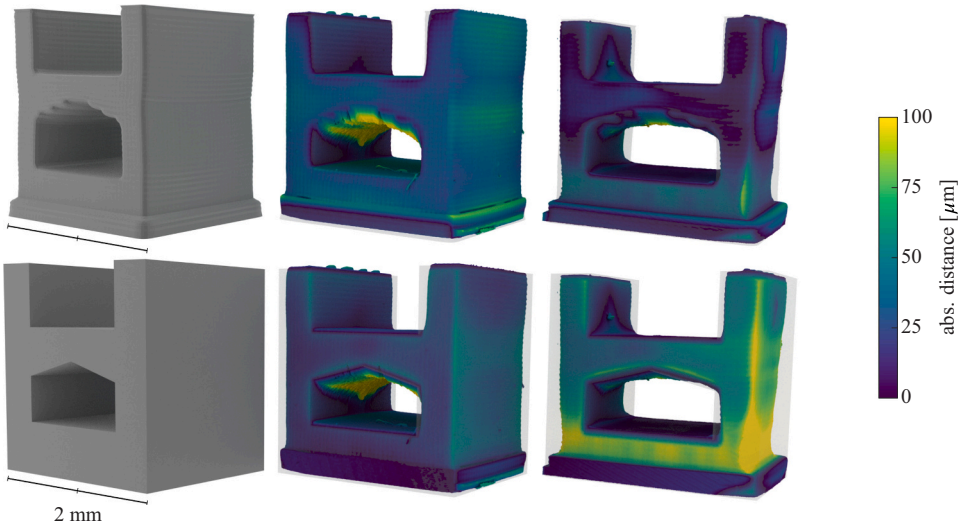

Fig. 16. Comparison of the simulated geometry with the printed samples (top row) and the target geometry with the printed samples (bottom row) for the H_2-shape. The range of the color bar is limited to 100 μm. For visual comparison, the CT images also include a transparent simulation/target geometry. (For interpretation of the references to color in this figure legend, the reader is referred to the web version of this article.)

5.2. H-shaped sample

The results for the H-shaped samples are depicted in Figs. 16 and 17 for the 2 and 3 mm wide sample, i.e. H_2 and H_3, respectively. When comparing the simulated, intended and printed results, the conclusions that were drawn for the T-sample also apply here. A large difference is present between the two printed H_2 samples in Fig. 16 due to process inaccuracies. This induces a large deviation from the target result in the rightmost printed sample, which is accurately captured by the simulation. For both printed shapes, the agreement on the predicted shape and deformation is excellent—with the predicted print-through in the overhang the sole exception. The outward warpage of the top pillars (further away from the waist itself) remains under-predicted.

5.3. Discussion

The simulation results in Sections 5.1 and 5.2 illustrate the need for predictive modeling and the added value of the developed framework. Some additional (more general) remarks need to be made.

Firstly, the limited reproducibility in the printed samples limits the correspondence with simulation results. It is key to identify any causes for a limited reproducibility—which might originate from e.g., the cleaning process or the characteristics of the irradiation source—and how to overcome these in practice [8]. In the current work, the samples are inspected right after removal from the print bed after printing, i.e. no post-curing is conducted. Note that this might have an additional influence on the resulting shape and (mechanical) properties [59].

The parameter characterization in this work relies on the identification of model parameters through numerical simulations. This implies that the modeling parameters may not be necessarily equal to the physical parameters and the model validation is of a qualitative nature, i.e. to identify whether the correct trends are captured through the multi-physical approach (with some more phenomenological ingredients). The mathematical formulation of the numerical framework is already involved from a parameter identification point of view. From a physical perspective, however, the level of detail is still limited. Due to the restricted fluid behavior, for example, the current method is not ideal for the prediction of printability of an overhang structure. The photopolymerization provides a final conversion between 0 and the peak conversion (p_∞), but it is independent of the depletion of the photoinitiator. Furthermore, the current implementation of oxygen inhibition ensures a good correspondence to the actual printed samples, but assumes full replenishment of oxygen from one irradiation to the next. This might appear oversimplified at first, but the agreement of the predictions indicate an adequate accuracy accompanying the phenomenological description of multiple effects. Possible effects are (but not limited to) the diffusion of oxygen through the resin, substitution of irradiated (but not solidified, i.e. liquid) resin during the recoating step and vitrification [24]. Whereas the phenomenological approach suits the goal of this work, enabling efficient component-scale simulations, a more accurate description might account for the presence of initiator and inhibitor (e.g., oxygen) species though additional ODEs [22,41]. Although in the current model, the interest lies in geometrical prediction—for a qualitative validation with printed specimens—the mechanical formulation would also allow for the prediction of residual stresses. Due to the purely linear elastic assumption—neglecting viscous effects—the predicted stresses might be considered an upper limit.

6. Conclusion

The characteristics of the AM apparatus and the material properties and process physics have a profound influence on the (quality of the) printed specimens. This work proposes a modeling framework for three-dimensional process simulation of the DLP VP process in order to predict the resulting geometry and the (unintended) deformations therein.

This is enabled through the development of a chemo-mechanical simulation framework that starts with the irradiation characteristics of the DLP system. To ensure that the resulting geometry is not affected by the computational domain, the process is simulated in an immersed region for which a (sufficiently large) volume of the resin vat is simulated. This is distinct from typical component-scale simulation frameworks that initiate from a pre-meshed geometrical realization of the target geometry that is selectively 'activated'. In this work, the model input consists of the sliced and pixelated (based on the resolution of the printer) cross-sections of the target geometry. As a result, the irradiation profile, combined with the polymerization and solidification characteristics, induce the resulting geometry prediction.

The validation of the developed framework is conducted by a direct comparison to printed samples. Although the printed samples show limited reproducibility, the simulated results correctly (both qualitatively and quantitatively) capture the main characteristic features that distinguish the printed samples from the target ones. Considering that the deformation is a direct result of the chemical shrinkage and the underlying linear momentum balance, the model can also be used as a predictive tool for residual stresses—through the constitutive relation. This might prove useful in the design of (complex shaped) geometries with respect to printability, e.g., to prevent the occurrence of cracks/delamination or excessive warpage. In addition, looking ahead, new

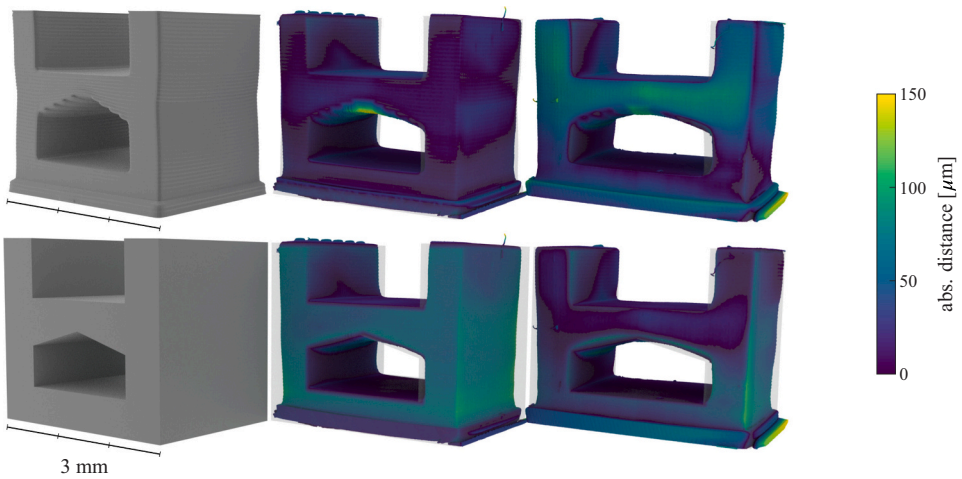

Fig. 17. Comparison of the simulated geometry with the printed samples (top row) and the target geometry with the printed samples (bottom row) for the H_3-shape. The range of the color bar is limited to 150 μm. For visual comparison, the CT images also include a transparent simulation/target geometry. (For interpretation of the references to color in this figure legend, the reader is referred to the web version of this article.)

paths to process optimization are opened as well as pre-manufacturing (digital) compensation of VP-inherent limitations with respect to geometric accuracy.

Future work should focus on alternative parameter identification strategies. Whereas the current work applies an iterative parameter optimization approach, ideally individual parameters should be identified from dedicated experiments. As a result, it is deemed feasible to uniquely identify the effect of individual process/material parameters through numerical simulation, e.g., changing the layer thickness or the addition of a dye. In turn, this will also provide the means to investigate the origin of reproducibility/repeatability issues in VP. To assess the shape characteristics of printed parts, the current formulation provides accurate results but the underlying stress prediction remains to be validated and, if needed, extended to a visco-elastic formulation. The physical formulation can be further extended by incorporation of temperature effects, UV (and/or thermal) post-curing, or by accounting for the presence of a (static) powder filler that induces e.g., light scattering and more involved mechanical behavior [12].

CRediT authorship contribution statement

Steyn Westbeek: Conceptualization, Data curation, Formal analysis, Investigation, Methodology, Software, Validation, Visualization, Writing - original draft. **Joris Remmers**: Conceptualization, Software, Funding acquisition, Methodology, Project administration, Supervision, Writing - review & editing. **Hans van Dommelen**: Conceptualization, Funding acquisition, Methodology, Project administration, Supervision, Writing - review & editing. **Hessel Maalderink**: Conceptualization, Methodology, Resources, Writing - review & editing. **Marc Geers**: Conceptualization, Funding acquisition, Methodology, Project administration, Supervision, Writing - review & editing.

Declaration of Competing Interest

The authors declare that they have no known competing financial interests or personal relationships that could have appeared to influence the work reported in this paper.

Acknowledgments

This study was funded by the Netherlands Organisation for Applied Scientific Research (TNO) and TU/e Impuls and was carried out in a collaboration between TU/e HTSC and TNO. The authors would like to extend special thanks to Marc van Maris and Niels Vonk for support with CT imaging and indentation experiments and Thomas Hafkamp for fruitful discussion on the effect of inhibition species in the polymerization process.

References

[1] F.P. Melchels, J. Feijen, D.W. Grijpma, A review on stereolithography and its applications in biomedical engineering, Biomaterials 31 (24) (2010) 6121–6130, https://doi.org/10.1016/j.biomaterials.2010.04.050.
[2] J.W. Halloran, Ceramic stereolithography: additive manufacturing for ceramics by photopolymerization, Annu. Rev. Mater. Res. 46 (2016) 10.1–10.22, https://doi.org/10.1146/annurev-matsci-070115-031841.
[3] A. Zocca, P. Colombo, C.M. Gomes, J. Günster, Additive manufacturing of ceramics: issues, potentialities, and opportunities, J. Am. Ceram. Soc. 98 (7) (2015) 1983–2001, https://doi.org/10.1111/jace.13700.
[4] P. Bartolo, J. Gaspar, Metal filled resin for stereolithography metal part, CIRP Ann. 57 (1) (2008) 235–238, https://doi.org/10.1016/j.cirp.2008.03.124.
[5] U. Scheithauer, E. Schwarzer, T. Moritz, A. Michaelis, Additive manufacturing of ceramic heat exchanger: opportunities and limits of the lithography-based ceramic manufacturing (LCM), J. Mater. Eng. Perform. 27 (1) (2018) 14–20, https://doi.org/10.1007/s11665-017-2843-z.
[6] Y. Huang, M.C. Leu, J. Mazumder, A. Donmez, Additive manufacturing: current state, future potential, gaps and needs, and recommendations, J. Manuf. Sci. Eng. 137 (2015), 014001, https://doi.org/10.1115/1.4028725.
[7] F. Liravi, S. Das, C. Zhou, Separation force analysis and prediction based on cohesive element model for constrained-surface stereolithography processes, CAD Comput. Aided Des. 69 (2015) 134–142, https://doi.org/10.1016/j.cad.2015.05.002.
[8] T.M. Hafkamp , G.E. van Baars , A.G. de Jager , L.F.P. Etman , Real-time feedback controlled conversion in vat photopolymerization of ceramics: a proof of principle, Addit. Manuf., https://doi.org/10.1016/j.addma.2019.06.026.
[9] K. Classens, T. Hafkamp, S. Westbeek, J. J. C Remmers, S. Weiland, Real-Time Nonlinear Tracking Control of Photopolymerization for Additive Manufacturing. in: 2021 IEEE American Control Conference (ACC), New Orleans, Louisiana, USA, 2021.
[10] K.H.J. Classens, T.M. Hafkamp, S. Westbeek, J.J.C. Remmers, S. Weiland, Multiphysical modeling and optimal control of material properties for photopolymerization processes, Addit. Manuf. 38 (2021), 101520, https://doi.org/10.1016/j.addma.2020.101520.
[11] S. Westbeek, J. van Dommelen, J. Remmers, M. Geers, Multiphysical modeling of the photopolymerization process for additive manufacturing of ceramics, Eur. J. Mech. A/Solids 71 (2018) 210–223, https://doi.org/10.1016/j.euromechsol.2018.03.020.
[12] S. Westbeek, J. Remmers, J. van Dommelen, M. Geers, Multi-scale process simulation for additive manufacturing through particle filled vat photopolymerization, Comput. Mater. Sci. 180 (2020), 109647, https://doi.org/10.1016/j.commatsci.2020.109647.
[13] I. Gibson, D. Rosen, B. Stucker, Additive Manufacturing Technologies, Springer New York, New York, NY, 2015, https://doi.org/10.1007/978-1-4939-2113-3.
[14] H. Narahara, F. Tanaka, T. Kishinami, S. Igarashi, K. Saito, Reaction heat effects on initial linear shrinkage and deformation in stereolithography, Rapid Prototyp. J. 5 (3) (1999) 120–128, https://doi.org/10.1108/13552549910278946.
[15] P.F. Jacobs, Rapid Prototyping & Manufacturing: Fundamentals of Stereolithography, Society of Manufacturing Engineers in Cooperation with the Computer and Automated Systems Association of SME, Dearborn, MI, 1992.
[16] R.S. Chambers, T.R. Guess, T.D. Hinnerichs, A phenomenological finite element model of stereolithography processing, Technical Reports March, Sandia National Labs., Albuquerque, 1996.
[17] M. Hossain, P. Steinmann, Degree of cure-dependent modelling for polymer curing processes at small-strain. Part I: consistent reformulation, Comput. Mech. 53 (4) (2013) 777–787, https://doi.org/10.1007/s00466-013-0929-5.
[18] V.V. Ivanov, C. Decker, Kinetic study of photoinitiated frontal polymerization, Polym. Int. 50 (1) (2001) 113–118, https://doi.org/10.1002/1097-0126(200101)50:1<113::aid-pi594>3.0.co;2-x.
[19] G. Terrones, A.J. Pearlstein, Effects of optical attenuation and consumption of a photobleaching initiator on local initiation rates in photopolymerizations, Macromolecules 34 (10) (2001) 3195–3204, https://doi.org/10.1021/ma001235y.
[20] G.A. Miller, L. Gou, V. Narayanan, A.B. Scranton, Modeling of photobleaching for the photoinitiation of thick polymerization systems, J. Polym. Sci. Part A Polym. Chem. 40 (6) (2002) 793–808, https://doi.org/10.1002/pola.10162.
[21] S.J. Oh, S.C. Lee, S.Y. Park, Photopolymerization and photobleaching of n-butyl acrylate/fumed silica composites monitored by real time FTIR-ATR spectroscopy, Vib. Spectrosc. 42 (2) (2006) 273–277, https://doi.org/10.1016/j.vibspec.2006.05.028.
[22] A.S. Jariwala, F. Ding, A. Boddapati, V. Breedveld, M.A. Grover, C.L. Henderson, D. W. Rosen, Modeling effects of oxygen inhibition in mask-based stereolithography, Rapid Prototyp. J. 17 (3) (2011) 168–175, https://doi.org/10.1108/13552541111124734.
[23] S.C. Ligon, B. Husár, H. Wutzel, R. Holman, R. Liska, Strategies to reduce oxygen inhibition in photoinduced polymerization, Chem. Rev. 114 (1) (2014) 557–589, https://doi.org/10.1021/cr3005197.
[24] J. Pierrel , A. Ibrahim , C. Croutxé-Barghorn , X. Allonas , Effect of the oxygen affected layer in multilayered photopolymers, Polym. Chem., https://doi.org/10.1039/C7PY00974G.
[25] J.T. Lin, H.W. Liu, K.T. Chen, D.C. Cheng, Modeling the kinetics, curing depth, and efficacy of radical-mediated photopolymerization: the role of oxygen inhibition, viscosity, and dynamic light intensity, Front. Chem. 7 (2019) 1–14, https://doi.org/10.3389/fchem.2019.00760.
[26] J. Christmann, C. Ley, X. Allonas, A. Ibrahim, C. Croutxé-Barghorn, Experimental and theoretical investigations of free radical photopolymerization: inhibition and termination reactions, Polymer 160 (2019) 254–264, https://doi.org/10.1016/j.polymer.2018.11.057.
[27] Y.-M. Huang, S. Kuriyama, C.-P. Jiang, Fundamental study and theoretical analysis in a constrained-surface stereolithography system, Int. J. Adv. Manuf. Technol. 24 (5–6) (2004) 361–369, https://doi.org/10.1007/s00170-003-1627-9.
[28] C.-P. Jiang, Y.-M. Huang, C.-H. Liu, Dynamic finite element analysis of photopolymerization in stereolithography, Rapid Prototyp. J. 12 (3) (2006) 173–180, https://doi.org/10.1108/13552540610670753.
[29] T. Wu. Theoretical Modeling and Experimental Characterization of Stress and Crack Development in Parts Manufactured Through Large Area Maskless Photopolymerization (Ph.D. thesis), Georgia Institute of Technology, 2014.
[30] Y. Yang, L. Li, J. Zhao, Mechanical property modeling of photosensitive liquid resin in stereolithography additive manufacturing: bridging degree of cure with tensile strength and hardness, Mater. Des. 162 (2019) 418–428, https://doi.org/10.1016/j.matdes.2018.12.009.
[31] N. Fang, C. Sun, X. Zhang, Diffusion-limited photopolymerization in scanning micro-stereolithography, Appl. Phys. A Mater. Sci. Process. 79 (8) (2004) 1839–1842, https://doi.org/10.1007/s00339-004-2938-x.
[32] Y. Tang, C. Henderson, J. Muzzy, D.W. Rosen, Stereolithography cure modelling and simulation, Int. J. Mater. Prod. Technol. 21 (4) (2004) 255, https://doi.org/10.1504/IJMPT.2004.004941.

[33] A. Boddapati. Modeling Cure Depth During Photopolymerization of Multifunctional Acrylates (M.Sc. thesis), Georgia Institute of Technology, 2010.
[34] H.-W. Kang, J.H. Park, D.-W. Cho, A pixel based solidification model for projection based stereolithography technology, Sens. Actuators A Phys. 178 (2012) 223–229, https://doi.org/10.1016/j.sna.2012.01.016.
[35] J.J.M. Knippenberg, S. Westbeek, M.G.D. Geers, J.J.C. Remmers, A framework for the thermomechanical analysis of AM processes, in preparation.
[36] T.J.R. Hughes. The Finite Element Method: Linear Static and Dynamic Finite Element Analysis, first ed, Dover Publications, 2000.
[37] R. de Borst, M.A. Crisfield, J.J.C. Remmers, C.V. Verhoosel. Non-Linear Finite Element Analysis of Solids and Structures, second ed, John Wiley & Sons, Ltd, Chichester, UK, 2012, https://doi.org/10.1002/9781118375938.
[38] A. Kozhevnikov, R. Kunnen, G. van Baars, H. Clercx, Influence of the recoating parameters on resin topography in stereolithography, Addit. Manuf. (2020), 101376, https://doi.org/10.1016/j.addma.2020.101376.
[39] M.M. Emami, D.W. Rosen, Modeling of light field effect in deep vat polymerization for grayscale lithography application, Addit. Manuf. 36 (2020), 101595, https://doi.org/10.1016/j.addma.2020.101595.
[40] Y. Tang, C.L. Henderson, J. Muzzy, D.W. Rosen, Stereolithography cure process modeling using acrylate resin, in: Proceedings of the Solid Freeform Fabrication Symposium, Austin, Texas, 2004, pp.612–623.
[41] M.M. Emami, D.W. Rosen, An improved vat photopolymerization cure model demonstrates photobleaching effects, in: Proceedings of the Solid Freeform Fabrication Symposium, Austin, Texas, 2018, pp.1940–1952.
[42] G. Odian, Principles of Polymerization, John Wiley & Sons, Inc., Hoboken, NJ, USA, 2004, https://doi.org/10.1002/047147875X.
[43] B. Metral, A. Bischoff, C. Ley, A. Ibrahim, X. Allonas, Photochemical study of a threecomponent photocyclic initiating system for free radical photopolymerization: implementing a model for digital light processing 3D printing, ChemPhotoChem 3 (11) (2019) 1109–1118, https://doi.org/10.1002/cptc.201900167.
[44] L. Flach, R.P. Chaftoff, A. Process, Model for nonisothermal photopolymerization with a laser light source. I: basic model development, Polym. Eng. Sci. 35 (6) (1995) 483–492, https://doi.org/10.1002/pen.760350605.
[45] J. Bennett, UV Measuring, Measuring UV curing parameters of commercial photopolymers used in additive manufacturing, Addit. Manuf. 18 (2017) 203–212, https://doi.org/10.1016/j.addma.2017.10.009.
[46] C. Decker, A.D. Jenkins, Kinetic approach of O2 inhibition in ultraviolet and laser induced polymerizations, Macromolecules 18 (1985) 1241–1244, https://doi.org/10.1016/j.ab.2011.10.035.
[47] H. Bikas, P. Stavropoulos, G. Chryssolouris, Additive manufacturing methods and modelling approaches: a critical review, Int. J. Adv. Manuf. Technol. 83 (2016) 389–405, https://doi.org/10.1007/s00170-015-7576-2.
[48] M.F. Gouge, P. Michaleris, Thermo-Mechanical Modeling of Additive Manufacturing, Elsevier, 2018, https://doi.org/10.1016/C2016-0-00317-0.
[49] N. Silikas, A. Al-Kheraif, D.C. Watts, Influence of P/L ratio and peroxide/amine concentrations on shrinkage-strain kinetics during setting of PMMA/MMA biomaterial formulations, Biomaterials 26 (2) (2005) 197–204, https://doi.org/10.1016/j.biomaterials.2004.02.028.
[50] S. Loshaek, T.G. Fox, Cross-linked polymers. I. Factors influencing the efficiency of cross-linking in copolymers of methyl methacrylate and glycol dimethacrylates 1, J. Am. Chem. Soc. 75 (14) (1953) 3544–3550, https://doi.org/10.1021/ja01110a068.
[51] C. Koplin, R. Jaeger, P. Hahn, A material model for internal stress of dental composites caused by the curing process, Dent. Mater. 25 (3) (2009) 331–338, https://doi.org/10.1016/j.dental.2008.08.007.
[52] P. Michaud, V. Pateloup, J. Tarabeux, A. Alzina, D. André, T. Chartier, Numerical prediction of elastic properties for alumina green parts printed by stereolithography process, J. Eur. Ceram. Soc., https://doi.org/10.1016/j.jeurceramsoc.2020.10.068.
[53] T.H. Pang, M.D. Guertin, H.D. Nguyen, Accuracy of stereolithography parts: mechanism and modes of distortion for a "Letter-H" diagnostic part, in: Solid freeform Fabrication Proceedings, 1995, 170–180.
[54] Y.M. Huang, J.Y. Jeng, C.P. Jiang, Increased accuracy by using dynamic finite element method in the constrain-surface stereolithography system, J. Mater. Process. Technol. 140 (1–3 SPEC.) (2003) 191–196, https://doi.org/10.1016/S0924-0136(03)00711-8.
[55] C. Koplin, M. Gurr, R. Mülhaupt, R. Jaeger, Shape accuracy in stereolithography: a material model for the curing behavior of photo-initiated resins, in: International User's Conference on Rapid Prototyping & Rapid Tooling & Rapid Manufacturing (Euro-uRapid), Berlin.
[56] K. Xu, Y. Chen, Mask image planning for deformation control in projection-based stereolithography process, J. Manuf. Sci. Eng. 137 (3) (2015), 031014, https://doi.org/10.1115/1.4029802.
[57] CloudCompare (version 2.10.1) [GPL software], 2019. ⟨http://www.cloudcompare.org/⟩.
[58] M.D. Goodner, H.R. Lee, C.N. Bowman, Method for determining the kinetic parameters in diffusion-controlled free-radical homopolymerizations, Ind. Eng. Chem. Res. 36 (1) (1997) 1247–1252, https://doi.org/10.1021/ie9605387.
[59] D. Wu, Z. Zhao, Q. Zhang, H.J. Qi, D. Fang, Mechanics of shape distortion of DLP 3D printed structures during UV post-curing, Soft Matter 15 (30) (2019) 6151–6159, https://doi.org/10.1039/c9sm00725c.